




Microstructure and mechanical properties of gadolinium- and misch metal-added Mg–Al alloy

Lavish Kumar Singh* , Prince Joseph, Amirthalingam Srinivasan, Uma Thanu Subramonia Pillai, Bellambettu Chandrasekhara Pai

Received: 17 August 2016/Revised: 21 October 2016/Accepted: 13 May 2017/Published online: 7 July 2017
© The Nonferrous Metals Society of China and Springer-Verlag Berlin Heidelberg 2017

Abstract The study investigates the effects of individual and combined additions of gadolinium (Gd) and misch metal (MM) on the microstructure and mechanical properties of Mg–4Al and Mg–9Al alloys. The results show that the additions significantly alter the microstructure and grain size of the base alloys. Mg–4Al based alloys have globular morphology, whereas Mg–9Al based alloys have dendritic morphology. The addition of alloying elements, Gd and MM, introduces rectangular-shaped Al_2Gd phase and needle-shaped $\text{Al}_{11}\text{RE}_3$ phase, respectively. The best mechanical properties at room temperature are shown by Mg–9Al–2Gd alloy with tensile strength and elongation of 214 MPa and 6.0%, respectively, whereas Mg–4Al–2Gd alloy exhibits the best properties at elevated temperature (150 °C) with tensile strength and elongation of 172 MPa and 14.0%, respectively. The study also reports the microhardness value of different phases along with the cast alloys. Eutectic $\text{Mg}_{17}\text{Al}_{12}$ phase shows the highest hardness (VHN 92) followed by lamellar $\text{Mg}_{17}\text{Al}_{12}$ (VHN 83) and α -Mg matrix (VHN 68).

Keywords Rare earth; Gadolinium; Alloying; Microstructure; Mechanical properties

1 Introduction

Magnesium alloys show tremendous potential in automotive, aerospace and railway industries due to their high specific strength, low density, enhanced electromagnetic shielding capacity, damping properties and proficient machinability [1]. The reduction in vehicle weight by 10% can lead to enhancement in fuel usage by 6%–8% [2], and 1 kg of weight reduction can reduce 17–20 kg of CO_2 emissions over a vehicle's lifetime [3]. Most of the commercially used Mg alloys are either Al or Zn alloyed. Alloying with Al improves castability and mechanical properties at room temperature. However, their applications are confined below 120 °C, due to the instability of β - $\text{Mg}_{17}\text{Al}_{12}$ phase at high temperature [4, 5]. It is also observed that Al content significantly affects the microstructure and, thereby, mechanical properties of Mg alloys. Therefore, it is important to study the influence of variation in Al content on Mg–Al alloys.

Several researchers have used combination of rare earth (RE) elements, known as misch metal (MM) as the alloying element. However, conflicting observations have been reported by different researchers for the phases formed when MM is added in Mg–Al alloy. Yong et al. [6] and Asl et al. [1] reported the presence of $\text{Mg}_{17}\text{Al}_{12}$ and $\text{Al}_{11}\text{RE}_3$ phases in MM-added Mg–Al alloy, whereas Wang et al. [7] and Zhang et al. [8] reported that no $\text{Mg}_{17}\text{Al}_{12}$ phase was present. Apart from $\text{Mg}_{17}\text{Al}_{12}$, researchers also reported the presence of secondary phases such as Al_3RE and Al_2RE in Mg–Al–MM alloys [8, 9]. Nevertheless, the addition of MM has always led to enhancement in mechanical properties. Mg–Al–RE alloys are being fabricated exclusively for applications at high-temperature AE42 (Mg–4Al–2RE). However, the creep resistance deteriorates rapidly as the temperature surpasses 150 °C due to partial decomposition

L. K. Singh*
Department of Metallurgical and Materials Engineering, Indian Institute of Technology Kharagpur, Kharagpur 721301, India
e-mail: lavish.singh2011@gmail.com

P. Joseph, A. Srinivasan, U. T. S. Pillai, B. C. Pai
Materials Science and Technology Division, National Institute for Interdisciplinary Science and Technology,
Trivandrum 695001, India

of $Al_{11}RE_3$ into $Mg_{17}Al_{12}$ and Al_2RE [10]. Mg–9Al-based alloy, AZ91, is the most extensively used die cast magnesium alloy for automotive components such as clutch housing, crankcase and oil pan. However, its application in several key automobile constructional components such as transmission and engine housing is restricted due to its comparatively low strength and inferior creep properties [11]. Therefore, in the present study, Mg–4Al and Mg–9Al alloys were selected as the base alloy.

Recently, high solubility RE elements such as Gd and Y have emerged as potential alloying elements for Mg alloys [11–13]. Gd shows high solubility (23.5 wt% at 548 °C, the eutectic temperature) in Mg, and therefore, a significant amount of Gd can be successfully added to achieve extensive solid-solution strengthening. Also, the solubility of Gd reduces drastically to 3.8 wt% at 200 °C, indicating that upon heat treatment, significant improvement in properties can be achieved via precipitation hardening. The Mg–Gd system is one of the candidates for a novel Mg-based light hardenable alloy with high creep resistance [14]. Wang et al. [15] reported that the tensile strength of Mg–2Al–1Zn at 200 °C increased by 35% upon alloying with 1.5 wt% Gd. However, few studies have been done on the effect of Gd addition in Mg–Al alloys. In the present work, six alloys, Mg–4Al, Mg–9Al, Mg–4Al–2Gd, Mg–9Al–2Gd, Mg–4Al–1MM–1Gd and Mg–4Al–2MM, were prepared and their mechanical properties were evaluated and correlated with the microstructure. These alloys were selected to study the effect of varying Al content, individual as well as combined effect of Gd and MM addition and the interaction of RE elements with low-Al- and high-Al-based magnesium alloys.

2 Experimental

2.1 Casting

Industrially pure magnesium ingot (99.95% purity) and aluminum ingot (99.95% purity) were selected for the base alloy casting. The required alloying elements Gd (99.98% purity), MM (99.95% purity) and Al-10% Mn

master alloy were added into it. Melting of Mg and Al was performed in a steel crucible in a resistance furnace. As the melting started, argon and sulfur hexafluoride were supplied as shielding gas with the volume ratio of 99.8:0.2 over the crucible containing melt. As the melt temperature approached 750 °C, Gd was added. Gentle stirring was done for 5 min to have uniform mixing of the additives within the melt. The melt was refined at 750 °C so as to eliminate the oxide covering formed over the exterior. Once the melt was settled, it was poured into a mold (metallic) which was preheated to 300 °C. Sulfur powder dusting was done while pouring in order to avoid oxidation and burning. The constitution of different elements in the cast alloys is presented in Table 1. Inductively coupled plasma spectrometer (ICP Plasmascan, model LABTAM 8410) was used to determine the composition of the cast alloys.

2.2 Microstructural characterization

Cylindrical samples with dimension of $\Phi 15$ mm \times 10 mm were prepared for microstructure analysis. The samples were initially ground up to 1000 grit paper followed by polishing with 0.25 μ m diamond paste. Etching was done by a solution of 5 ml acetic acid, 6 g picric acid, 10 ml H_2O and 100 ml ethanol. The microstructure was quantitatively analyzed using an Image analyzer (Leica 2001) in conjunction with the Leitz–Metalloplan optical microscope (OM). The surface was examined by scanning electron microscope (SEM JEOL, JSM 35C) in order to identify the distribution and morphology of different phases present in the cast samples. Energy-dispersive spectroscope (EDS), coupled with SEM, was used to determine the compositions of different phases and intermetallics formed within the matrix. X-ray diffraction (XRD) analysis was performed using Cu $K\alpha$ radiation in Phillips PW1710 powder diffractometer. The grain size was measured by the linear-intercept method. Twenty readings at randomly selected places were recorded for the same. Transmission electron microscope (TEM, JEM-2100 HRTEM, JEOL, Japan) was used to identify different phases and dislocations generated within the samples.

Table 1 Chemical compositions of experimental alloys (mass fraction, %)

Alloy code	Alloy	Mg	Al	Gd	MM(Ce 50%, La 25%, Nd 18%, Pr 6%, other 1%)
AG40	Mg–4Al	Bal.	4.08	–	–
AG90	Mg–9Al	Bal.	9.18	–	–
AG42	Mg–4Al–2Gd	Bal.	3.86	2.11	–
AG92	Mg–9Al–2Gd	Bal.	9.12	2.14	–
AGM11	Mg–4Al–1MM–1Gd	Bal.	4.07	1.04	1.12
AGM02	Mg–4Al–2MM	Bal.	4.02	–	1.98

2.3 Mechanical testing

The tensile samples were machined out of the castings as per ASTM E8 specifications. Instron universal testing machine (Instron Corp., England) was used to carry out the tensile test at room temperature as well as at high temperature (150 °C) with a strain rate of 0.0013 s^{-1} . At least five samples were tested in each condition. INDENTEC hardness machine was used for Brinell hardness measurement. The samples were polished up to 600 grit paper. The indenter ball diameter was 2.5 mm, and the load was fixed at 613 N with a dwell time of 20 s. For microhardness measurement, a Vickers microhardness tester was used. Load of 0.25 N was applied with a dwell time of 10 s. Nanoindentation (TI 950, Triboindenter, Hysitron Inc., USA) was performed in control loading rate mode to assess the effective elastic modulus using the standard Berkovich tip. The indentation cycle consists of a loading segment of 10 s, followed by a load holding segment of 3 s at the maximum applied load of 8000 μN and an unloading segment of 10 s.

3 Results and discussion

3.1 Microstructure

XRD patterns of the cast alloys are illustrated in Fig. 1. The XRD patterns of Mg–4Al and Mg–9Al alloys confirm

that they contain two phases, α -Mg and β -Mg₁₇Al₁₂, which coincides with the earlier studies [16–18]. When Mg–4Al alloy was alloyed with Gd and MM, apart from the earlier observed phases, Al₂Gd and Al₁₁RE₃ phases were formed, respectively. XRD pattern of Mg–4Al–1MM–1Gd alloy (not shown here) shows no peaks of Al₂Gd and Al₁₁RE₃ phase which is due to the presence of these phases in very small amount. Figures 2 and 3 show OM images of as-cast Mg–4Al and Mg–9Al alloys obtained at low magnification, giving the morphology and distribution of different phases in the alloys. SEM images of the alloys are shown in Fig. 4. From the OM and SEM images, it can be seen that Mg–4Al (Fig. 2a) and Mg–9Al alloys (Figs. 3a, 4a) consist of β -

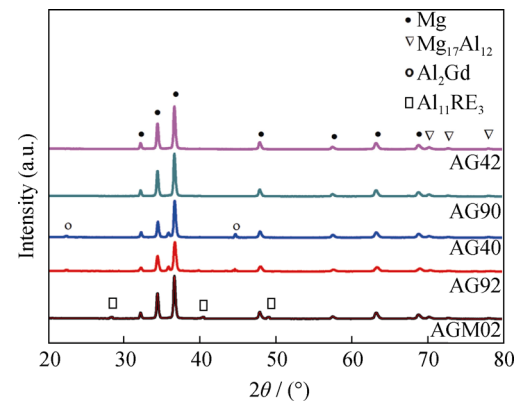


Fig. 1 XRD patterns of the alloys

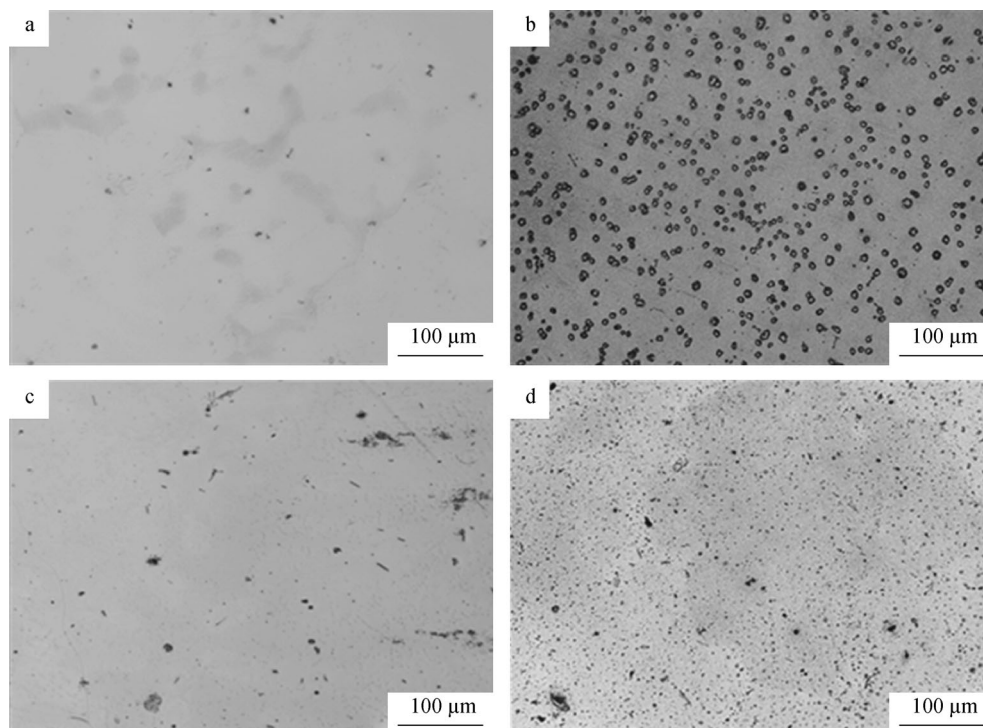


Fig. 2 OM images of as-cast Mg–4Al-based alloys: **a** Mg–4Al alloy, **b** Mg–4Al–2Gd alloy, **c** Mg–4Al–2MM alloy and **d** Mg–4Al–1MM–1Gd alloy

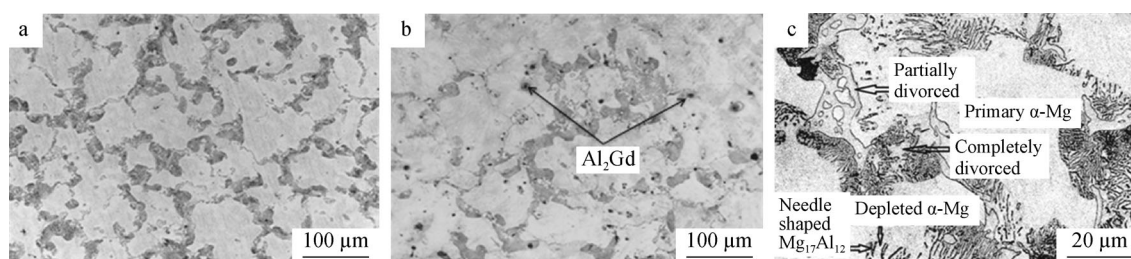


Fig. 3 OM images of as-cast Mg-9Al-based alloys: **a** Mg-9Al alloy, **b** Mg-9Al-2Gd alloy, and **c** High-magnified micrograph of Mg-9Al alloy

Mg₁₇Al₁₂ phase in a matrix of α -Mg solid solution which complements the XRD findings. According to Mg-Al phase diagram, Mg₁₇Al₁₂ phase should appear when Al content reaches 13 wt% [17]; but due to non-equilibrium cooling, the eutectic phase is visible in Mg-4Al alloy and has a globular morphology. The microstructures of Mg-9Al-based alloys consist of two classes of Mg₁₇Al₁₂ particles with the same composition (Fig. 3c). One is massive Mg₁₇Al₁₂ particles with irregular shape (Fig. 5a), and the other one is small needle-like lamellar particles (Fig. 6a). The microstructure mainly contains divorced eutectic along with sparingly distributed partially divorced structure. The non-equilibrium cooling during solidification in the present study contributes to the formation of divorced eutectic structure. There was an emergence of lamellar precipitates around the massive β -phase from the super-saturated eutectic α -solid solution due to the continuous cooling following the eutectic temperature [16].

When Gd was added in Mg-4Al and Mg-9Al alloys, a rectangular-shaped precipitate was formed, which upon EDS analysis (Fig. 5b) is confirmed to be Al₂Gd. Figures 2b and 4b show distribution of Al₂Gd phase in Mg-4Al-2Gd alloy. Similarly, Figs. 3b and 4c show distribution of Al₂Gd phase in Mg-9Al-2Gd alloy. Wang et al. [15] also observed rectangular-shaped precipitate in Mg-2Al-1Zn-2.9Gd alloy, as observed in the present study, and confirmed it to be Al₂Gd. When MM was added in Mg-4Al alloy, a needle-shaped phase is formed (Fig. 2c). However, in Mg-4Al-1MM-1Gd alloy, both needle-shaped and rectangular-shaped phases are observed (Figs. 2d and 4d). EDS analysis confirms the needle-shaped phase to be Al₁₁RE₃ (Fig. 5c). Using image analyzer, it was found that the volume ratio of Al₂Gd phase to Al₁₁RE₃ phase in AGM411 alloy is 7:3. This may be attributed to the high crystallizing temperature of Al₂Gd phase as compared to Al₁₁RE₃ phase. Moreover, owing to its high crystallization temperature, more amount of Al is consumed in the formation of Al₂Gd phase, consequently, leaving less amount of Al for the formation of Al₁₁RE₃ phase. The addition of MM and Gd also leads to depletion in the aggregation of β -Mg₁₇Al₁₂ phase. The content of Mg₁₇Al₁₂ phase in Mg-9Al alloy reduces from 15.36 vol% to 9.92 vol% in Mg-

9Al-2Gd alloy. The content of Al₂Gd phase in Mg-9Al-2Gd was measured to be 2.96 vol%. When Gd was added in Mg-Al alloy, Al-Gd intermetallic is formed rather than Mg-Gd intermetallic. The preference of Al over Mg is because the larger the difference in electronegativity is, the more the tendency is to form an intermetallic compound. The difference in electronegativity is 0.41 for Al and Gd, whereas it is 0.11 in case of Mg and Gd. Therefore, a considerable amount of Al is consumed in forming an Al-Gd intermetallic, and less amount of Al is available for the formation of Mg₁₇Al₁₂ phase. This leads to a reduction in the amount of Mg₁₇Al₁₂ phase upon alloying.

The average grain sizes of Mg-4Al, Mg-9Al, Mg-4Al-2MM Mg-4Al-2Gd and Mg-9Al-2Gd varied as 305, 254, 244, 213 and 181 μ m, respectively. However, the reduction in grain size was most significant for Mg-4Al-1MM-1Gd alloy (202 μ m). This is attributed to aggregation of significant amount of MM and Gd atoms at the solid-liquid interface. As they interact and reduce the solid solubility of each other in α -Mg matrix, more effective undercooling occurs at the interface [19, 20].

RE elements are known to have high growth restriction factor (GRF). Grain refining ability of solute atoms increases as GRF increases [17]. The GRF is expressed as [16]:

$$\text{GRF} = \sum m \times c (k - 1) \quad (1)$$

where m is liquidus line's slope, c denotes the initial composition, and k represents the element equilibrium partition coefficient. Elements with high GRF produce fast undercooling as their crystal grows. Therefore, the liquid around nucleants undercools quickly, allowing a stable nucleus to form on the nucleant particle [16]. In Mg-4Al-2Gd and Mg-9Al-2Gd alloys, the total solute content (Al + Gd) is 6 and 11 wt%, respectively. Therefore, it can be seen that Gd-added alloys have smaller grain size compared to their respective base alloys. Gd and Mg have similar structure (hcp), nearly the same atomic radii and lattice parameter which render Gd to act as a site for heterogeneous nucleation for α -Mg phase. The difference in atomic radii and lattice constant of Mg and Gd is 0.018 and 0.043 nm, respectively [21]. The alloys containing Gd

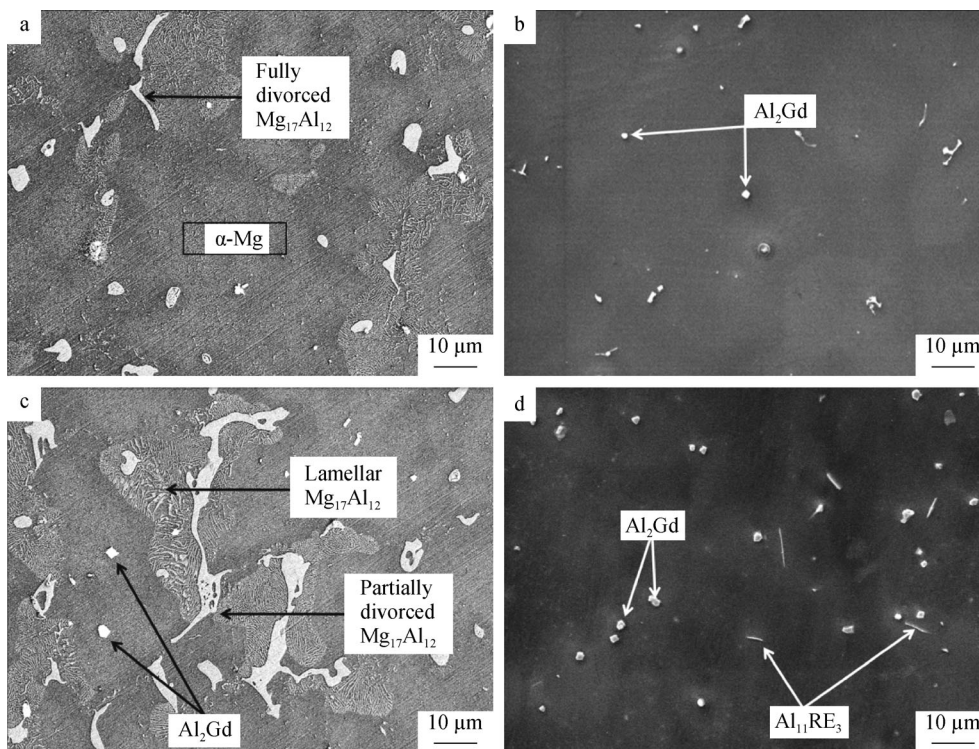


Fig. 4 SEM images of as-cast alloys: **a** Mg–9Al alloy, **b** Mg–4Al–2Gd alloy, **c** Mg–9Al–2Gd alloy, and **d** Mg–4Al–1MM–1Gd alloy

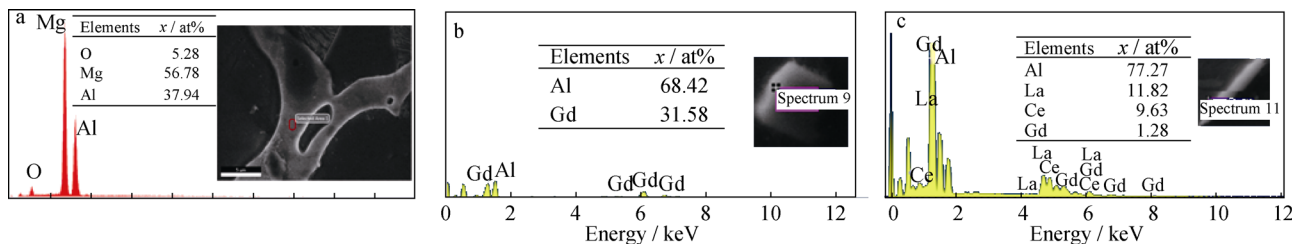


Fig. 5 SEM images and EDS results of **a** phase with dendritic morphology (Mg₁₇Al₁₂), **b** rectangular-shaped phase (Al₂Gd) and **c** needle-shaped phase (Al₁₁RE₃)

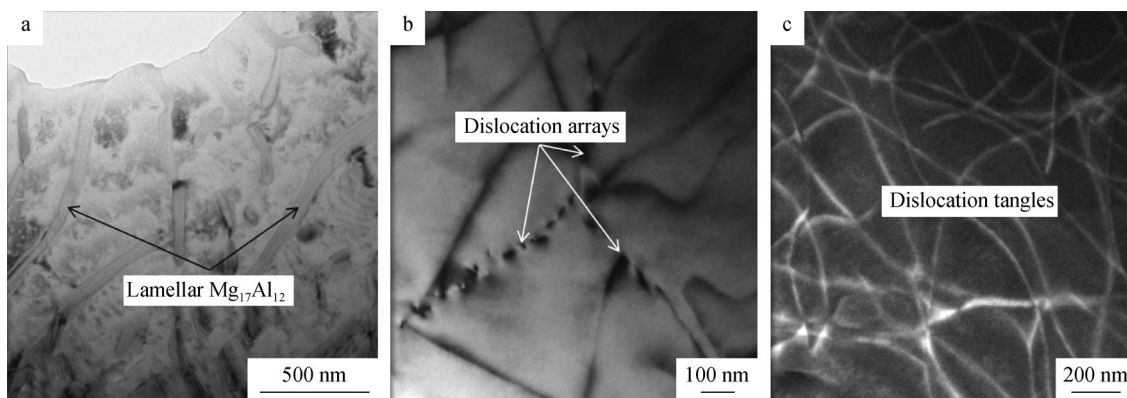


Fig. 6 TEM images showing **a** lamellar Mg₁₇Al₁₂ phase, **b** dislocation arrays and **c** dislocation tangles in Mg–9Al-based alloys

have relatively smaller grain size compared to MM-added alloys because Ce, the major constituent of MM, has fcc crystal structure. Also, the difference in atomic radii of Mg–Ce is 0.021 nm and the difference in lattice constant is 0.195 nm [21] which accounts for comparatively higher disregistry in MM-added alloys.

In spite of alloying, the observed reduction in grain size is not very significant in the present study. RE elements segregate to form secondary phases after the primary phase nucleates; therefore, they have little impact on nucleation of the primary phase [22]. Moreover, in gravity casting, the cooling rate is very low (about 80 K·s⁻¹) and this results in little undercooling which is detrimental for grain refinement. The free energy associated with the formation of a nucleus (ΔG_n) and the critical radius of a nucleus (r_o) are related to the undercooling (ΔT) as [23]:

$$\Delta G = A/\Delta T^2 \quad (2)$$

$$r_o = 2\gamma_{sl}/S_v\Delta T \quad (3)$$

where A is constant for a particular nucleating system, γ_{sl} is the interfacial energy between liquid and nucleation particles, and S_v is the entropy of fusion of the nucleation per unit volume. Therefore, the values of free energy and the critical radius for nucleus formation are relatively high in gravity casting due to low undercooling which results in low nucleation rate and hence less grain refinement. However, according to Qiu and Zhang [24], large ΔT also raises the growth rate of the new crystals and causes the release of more latent heat. This may reduce the undercooling and eventually may terminate the nucleation process if $\Delta T > 0$. Therefore, there is an optimum size of the active nucleation particle, leading to the finest grains.

3.2 Mechanical properties

Table 2 illustrates the mechanical properties of the studied alloys. The room temperature (RT) mechanical properties

Table 2 Mechanical properties of the studied alloy at room temperature and at 150 °C

Alloy code	Room temperature properties			High-temperature properties (150 °C)		
	YS/MPa	UTS/MPa	Elongation/%	YS/MPa	UTS/MPa	Elongation/%
AG40	97	173	4.6	76	152	10.3
AG90	108	184	5.1	73	148	11.5
AG42	118	208	6.1	98	172	14.0
AG92	112	214	6.0	89	162	10.5
AGM411	106	191	5.2	90	163	11.2
AGM402	99	184	5.0	79	155	9.8

of Mg–9Al alloy is better than those of Mg–4Al alloy; the tensile strength being 184 and 173 MPa, respectively. However, opposite behavior is observed at 150 °C, where the respective tensile strength is 148 and 152 MPa. Therefore, it can be inferred that increasing Al content exerts a positive effect on RT mechanical properties, whereas it is detrimental to high-temperature (HT) properties. The solubility of Al in α -Mg is constant at a particular temperature; so, the excess Al which cannot dissolve into α -Mg exists as β -Mg₁₇Al₁₂ in the eutectic mixture. Therefore, the content of β -Mg₁₇Al₁₂ is more in Mg–9Al as evident from XRD patterns and micrographs. β -Mg₁₇Al₁₂ phase causes an improvement in RT mechanical properties as it is very hard at ambient temperature. Gharghouri et al. [25] experimentally measured Young's modulus and yield stress of Mg₁₇Al₁₂ precipitates in Mg alloy and obtained the values as 80 and 1 GPa, respectively. However, owing to the following reasons, Mg₁₇Al₁₂ precipitates are detrimental for HT properties: (1) low melting point of Mg₁₇Al₁₂ phase (437 °C) [26], (2) rapid diffusion rate of Al in Mg matrix at high temperature [26], and as the temperature rises beyond 100 °C, Mg₁₇Al₁₂ no more hinders dislocation movement [27], and (3) Mg₁₇Al₁₂ has a cubic crystal structure which makes it incoherent with hcp magnesium matrix [28].

There are many phenomena whose effect sums up to define the mechanical properties of a particular alloy, yet they can primarily be categorized into three categories: (1) grain size reduction, (2) solid-solution strengthening, and (3) dispersion strengthening. Figure 7 shows the schematic diagram of strengthening mechanisms that takes place in the studied alloys.

3.2.1 Hall–Petch strengthening

The effect of grain size on yield strength (YS) is described by Hall–Petch formula which is expressed as [29]:

$$\sigma_y = \sigma_0 + Kd^{-1/2} \quad (4)$$

where σ_y represents YS of the alloy, σ_0 represents the “friction stress” representing the overall resistance of the crystal lattice to dislocation movement, K represents the “locking parameter” which measures the relative hardening contribution of the grain boundaries, and d represents the average grain diameter. The value of K usually increases with the decrease in the number of glide systems. Magnesium, possessing hcp structure, has fewer glide systems than the metals with bcc structure or fcc structure. So, Mg alloys have a large value of K which significantly affects YS in spite of little alteration in grain size. The number of dislocations in the pile up at the grain boundary decreases as the grain size reduces. Therefore, in order to

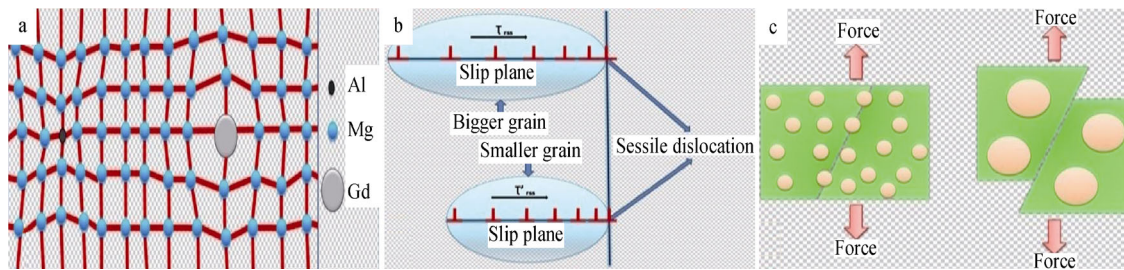


Fig. 7 Schematic representation of different strengthening mechanisms taking place in studied alloys: **a** solid-solution strengthening, **b** Hall–Petch strengthening and **c** dispersion strengthening

move a dislocation across a grain boundary, the magnitude of the applied stress needs to be increased which in turn increases YS [30]. The variation in tensile properties clearly shows Hall–Petch effect. The tensile strength and YS are high for alloys with small grain size. Mg–9Al–2Gd alloy with the smallest grain size (181 μm) exhibits the highest tensile strength (214 MPa) and high YS (112 MPa). Table 3 shows the Brinell and Vickers hardness values of the studied alloys. It is observed that Mg–9Al-based alloys exhibit high hardness compared to Mg–4Al-based alloys. The combined effect of grain refinement and existence of hard intermetallics lead to substantial increase in hardness of Gd-added Mg–Al alloys. When the grain size reduces, the grain boundary area increases, and since the strength of grain boundaries at RT is higher than that of the matrix, the hardness increases [31]. The grain boundary area possesses high hardness because it is a non-crystalline region, whereas the matrix is a crystalline region. Table 4 shows microhardness values of different phases present in Mg–9Al-based alloys. Eutectic $\text{Mg}_{17}\text{Al}_{12}$ phase shows the highest hardness (VHN 92) followed by lamellar $\text{Mg}_{17}\text{Al}_{12}$ (VHN 83) and α -Mg matrix (VHN 68). Figure 8a shows the microhardness indent over different phases. Elastic modulus of the cast alloys was evaluated via load versus displacement curve (Fig. 8b) generated during nanoindentation test. It is observed that elastic modulus values of the alloys follow the hardness trend.

Table 3 Hardness and elastic modulus of the studied alloys

Alloy code	Brinell hardness (BHN)	Vickers hardness (VHN)	Elastic modulus/GPa
AG40	47	62	39
AG90	64	74	49
AG42	55	71	47
AG92	67	79	54
AGM411	52	66	44
AGM402	48	65	43

Table 4 Microhardness of observed phases in Mg–9Al–2Gd alloy (VHN)

α -Mg	Lamellar $\text{Mg}_{17}\text{Al}_{12}$	Eutectic $\text{Mg}_{17}\text{Al}_{12}$
68	83	92

3.2.2 Solid-solution strengthening

Fleischer [32] and Labusch [33] formulated equation that relates the strength ($\sigma_{0.2} = 0.2\%$ proof strength) of a metallic material to the solute concentration (c). Both equations suggest the following relation:

$$\sigma_{0.2} \propto c^n \quad (5)$$

where $n = 1/2$ [32] and $2/3$ [33]. The relation proposes a simple relation that the 0.2% proof strength is proportional to the concentration of the solute. In the present study, the solute atoms (Al, MM and Gd) cause lattice strain which anchor dislocations, and therefore, more force is required to move the dislocations, thereby, increasing the strength. The effect of solid-solution strengthening can also be related with bond energy. Upon analyzing valence electron structures via empirical electron theory (EET) of solids and molecules, Guo et al. [34] suggested that the bond energy of Mg–Y is always higher than that of Mg–Al. The electronic structure of Y and Gd is similar. Therefore, it is logical to assume that the bond energy between Mg and Gd is greater than that between Mg and Al, and the higher the bond energy is, the better the solid-solution strengthening effect is.

3.2.3 Dispersion strengthening

The precipitates of $\text{Mg}_{17}\text{Al}_{12}$, Al_2Gd and $\text{Al}_{11}\text{RE}_3$ exert dispersion strengthening at elevated temperature. The increment in critical resolved shear stress (Orowan increment) required for dislocations to bypass the obstacles is expressed by the following expression [35]:

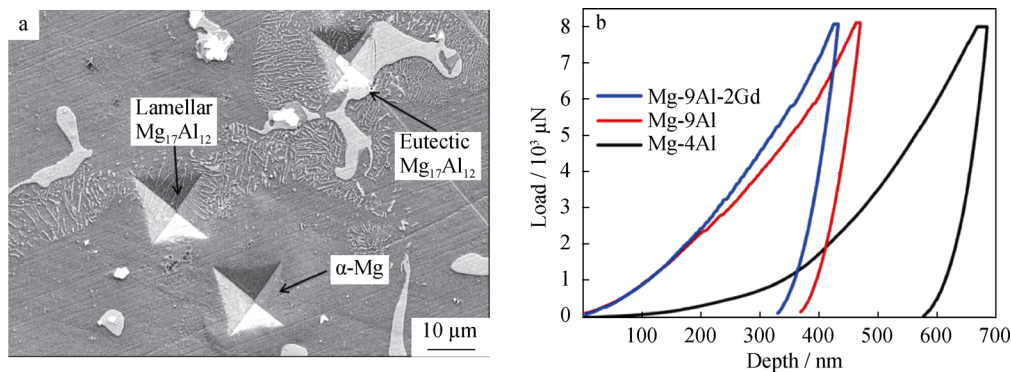


Fig. 8 SEM image showing hardness indent (Vickers) on different phases formed in Mg–9Al2Gd alloy **a** and load versus displacement curve for studied alloys **b**

$$\Delta\tau = \frac{Gb}{2\pi\lambda\sqrt{1-\nu}} \ln \frac{d_p}{r_0} \quad (6)$$

where $\Delta\tau$ is the dispersion strengthening induced Orowan increment, G is the matrix phase's rigidity modulus, b is the magnitude of the Burgers vector of the slip dislocations, λ is the effective obstacle spacing, d_p is the point obstacles' mean planar diameter, and r_0 is the dislocations' core radius. The equation implies that critically resolved shear stress (CRSS) $\propto 1/\lambda \propto G$. As discussed earlier, there were a greater number of Al_2Gd precipitates than $\text{Al}_{11}\text{RE}_3$ precipitates, so $\lambda (\text{Al}_{11}\text{RE}_3) > \lambda (\text{Al}_2\text{Gd})$. Also, $G (\text{Gd}) = 22 \text{ GPa} > G (\text{Ce}) = 14 \text{ GPa}$ [22]. Therefore, Gd-containing alloys are more dispersion hardened, being maximum for Mg–9Al–2Gd as it contains greater number of precipitates ($\text{Al}_2\text{Gd} + \text{Mg}_{17}\text{Al}_{12}$) due to high availability of Al. Figure 6b, c shows dislocation activities in Mg–9Al alloy in the form of dislocation arrays and dislocation tangles.

The degree of improvement in tensile properties is more for Gd-added alloy (Mg–4Al–2Gd) than for the alloy containing MM (Mg–4Al–2MM). The shape of the second phase may be one of the reasons for this variation. $\text{Al}_{11}\text{RE}_3$ phase formed in Mg–4Al–2MM is needle-shaped which becomes a center of stress concentration and results in easy initiation and extension of cavities, thereby deteriorating tensile properties. The cavities grow in size as the temperature increases, which further deteriorate the HT tensile properties. On the other hand, Al_2Gd phase formed in Mg–4Al–2Gd is rectangular in shape where the degree of stress concentration will be less. It is the detrimental effect of needle-shaped phase that causes the decrease in elongation for Mg–4Al–2MM alloy. Moreover, the increase in elongation is marginal at RT and HT in case of Mg–4Al–1MM–1Gd. The presence of the needle-shaped $\text{Al}_{11}\text{RE}_3$ phase in Mg–4Al–1MM–1Gd, although in less amount compared to Mg–4Al–2MM easily becomes a site for crack initiation and propagation, leading to marginal increment in elongation.

4 Conclusion

The microstructure and mechanical properties of gravity cast Mg–4Al, Mg–9Al, Mg–4Al–2Gd, Mg–9Al–2Gd, Mg–4Al–1MM–1Gd and Mg–4Al–2MM alloys were investigated to study the effect of alloying Al, Gd and MM on Mg–Al alloy system. Addition of Gd in Mg–Al alloys causes marginal grain refinement along with significant changes in microstructure. Addition of Gd and MM leads to reduction in amount of $\text{Mg}_{17}\text{Al}_{12}$ phase and the emergence of a rectangular-shaped Al_2Gd phase and needle-shaped $\text{Al}_{11}\text{RE}_3$ phase, respectively. Mg–4Al-based alloys have globular morphology, whereas Mg–9Al-based alloys have dendritic morphology. Addition of Gd and MM causes significant improvement in mechanical properties. Mg–9Al–2Gd alloy shows the best mechanical properties at room temperature, but the best high-temperature property is exhibited by Mg–4Al–2Gd alloy. This shows that increasing Al content has a positive influence on room temperature properties, but is detrimental for high-temperature properties. The degree of improvement in tensile properties is more for Gd-added alloys as compared to MM-added alloys. The shape of the second phase is one of the reasons for this variation. $\text{Al}_{11}\text{RE}_3$ phase is needle-shaped which becomes a center of stress concentration and results in easy initiation and extension of cavities.

References

- [1] Asl KM, Tari A, Khomamizadeh F. The effect of different content of Al, RE and Si element on the microstructure, mechanical and creep properties of Mg–Al alloys. *Mater Sci Eng A*. 2009;523(1–2):1.
- [2] Saidpour H. Lightweight High Performance Materials for Car Body Structures. In: *NTI Technology Conference*, London, 2004:14.
- [3] Mustafa KK. Magnesium and its alloys applications in automotive industry. *Int J Adv Manuf Technol*. 2008;39(9):851.

- [4] Xiaoquin Z, Quodong W, Yizhen L, Yanping Z, Wenjiang D, Yunhu Z. Influence of beryllium and rare earth additions on ignition-proof magnesium alloys. *J Mater Proc Tech.* 2001; 112(1):17.
- [5] Friedrich H, Schumann S. Research for a “new age of magnesium” in the automotive industry. *J Mater Proc Technol.* 2001; 17(3):276.
- [6] Yong YI, Yongge F, Yongjian T. Effect of lanthanum-praseodymium-cerium mischmetal on mechanical properties and microstructure of Mg–Al alloys. *J Wuhan Univ Technol.* 2011;26(1):102.
- [7] Wang J, Shi N, Wang L, Cao Z, Wang L, Li J. Effect of zinc and mischmetal on microstructure and mechanical properties of Mg–Al–Mn alloy. *J Rare Earth.* 2010;28(5):794.
- [8] Zhang J, Liu S, Leng Z, Zhang M, Meng J, Wu R. Microstructures and mechanical properties of heat-resistant HPDC Mg–4Al-based alloys containing cheap misch metal. *Mater Sci Eng A.* 2011;528(6):2670.
- [9] Rzychon T, Kielbus A. Effect of rare earth elements on the microstructure of Mg–Al alloys. *JAMME.* 2006;17(1–2):149.
- [10] Xue S, Sun YS, Ding SS, Bai Q, Bai J. Effects of calcium additions on microstructure and creep behaviour of AE42 alloy. *Mater Sci Technol.* 2008;21(7):847.
- [11] Luo A. Recent magnesium alloy development for elevated temperature applications. *Int Mater Rev.* 2004;49(1):13.
- [12] Li KJ, Li QA, Jing XT, Chen J, Zhang XY. Effects of Sb, Sm, and Sn additions on the microstructure and mechanical properties of Mg–6Al–1.2Y–0.9Nd alloy. *Rare Met.* 2009;28(5):516.
- [13] Wang QD, Peng JG, Michel S, Blandin JJ. Effects of aging on the microstructures and mechanical properties of extruded AM50 + xCa magnesium alloys. *Rare Met.* 2006;25(4):377.
- [14] Cizek J, Prochazka I, Smola B, Stulikova I, Ocenasek V. Influence of deformation on precipitation process in Mg–15 wt%Gd alloy. *J Alloys Compd.* 2007;430(1–2):92.
- [15] Wang X, Du W, Liu K, Wang Z, Li S. Microstructure, tensile properties and creep behaviors of as-cast Mg–2Al–1Zn–xGd ($x = 1, 2, 3,$ and 4 wt%) alloys. *J Alloys Compd.* 2012;522:78.
- [16] Dargusch MS, Pettersen K, Nogita K, Nave MD, Dunlop GL. The effect of aluminium content on the mechanical properties and microstructure of die cast binary magnesium–aluminium alloys. *Mater Trans.* 2006;47(4):977.
- [17] Dahle AK, Lee YC, Nave MD, Schaffer PL, StJohn DH. Development of the As-cast microstructure in magnesium–aluminium alloys. *J Light Met.* 2001;1:61.
- [18] Ma YT, Zhang XG, Liu HB, Meng LG. Effects of Er on the microstructure and properties of AZ31 magnesium alloy prepared via the EMS process. *Rare Met.* 2010;29(4):339.
- [19] Peng QM, Wu YM, Fang DQ, Meng J, Wang LM. Microstructures and properties of Mg–7Gd alloy containing Y. *J Alloys Compd.* 2007;430(1–2):252.
- [20] Rokhlin LL, Dobatkina TV, Nikitina NI. Constitution and properties of the ternary magnesium alloys containing two rare-earth metals of different subgroups. *Mater Sci Forum.* 2003; 419:291.
- [21] Lee YC, Dahle AK, StJohn DH. The role of solute in grain refinement of magnesium. *Metall Mater Trans A.* 2000;3(11): 2895.
- [22] Luo A. Understanding the solidification of magnesium alloys. In: *Third International Magnesium Conference.* (Eds. G.W. Lorimer), Manchester, UK. 1996. 449.
- [23] Reed-Hill RE. *Physically Metallurgy Principles.* 2nd ed. New York: Litton Educational Publishing; 2008.
- [24] Qiu D, Zhang MX. Effect of active heterogeneous nucleation particles on the grain refining efficiency in an Mg–10 wt% Y cast alloy. *J Alloys Compd.* 2009;488(1):260.
- [25] Gharghoury MA, Weatherly GC, Embury JD. The interaction of twins and precipitates in a Mg–7.7at.% Al alloy. *Philos Mag A.* 1998;78(5):1137.
- [26] Mahmudi R, Kabirian F, Nematollahi Z. Microstructural stability and high-temperature mechanical properties of AZ91 and AZ91 + 2RE magnesium alloys. *Mater Des.* 2011;32(5):2583.
- [27] Mordike BL, Ebert T. Magnesium: properties—applications—potential. *Mater Sci Eng A.* 2001;302(1):37.
- [28] Regev M, Aghoin E, Rosen A, Bamberger M. Creep studies of coarse-grained AZ91D magnesium castings. *Mater Sci Eng A.* 1998;252(1):6.
- [29] Caceres CH, Davidson CJ, Griffiths JR, Newton CL. Effects of solidification rate and ageing on the microstructure and mechanical properties of AZ91 alloy. *Mater Sci Eng A.* 2002; 325(1–2):344.
- [30] Dieter GE. *Mechanical Metallurgy.* 3rd ed. London: McGraw–Hill Book Company; 1986. 182.
- [31] Hultgren R, Mitchell DW. Grain refinement of magnesium alloys without superheating. *Trans AIME.* 1945;161:323.
- [32] Fleischer RL. Solution hardening. *Acta Metall.* 1961;9(11):996.
- [33] Labusch R. A statical theory of solid solution hardening. *Phys Status Solidi B.* 1970;41(2):659.
- [34] Guo X, Li P, Zeng DJ. Electron theory research in Mg–Y Alloy. *Chin Rare Earth Soc.* 2003;21(6):672.
- [35] Ardell AJ. Precipitation hardening. *Metall Mater Trans A.* 1985; 16(12):2131.